

Structure of ZnO Nanorods using X-Ray Diffraction

Marci Howdysshell

Office of Science, Science Undergraduate Laboratory Internship

Albion College

Stanford Linear Accelerator Center

Stanford, California

10 August 2007

Prepared in partial fulfillment of the requirements of the Office of Science, U.S. Department of Energy's Science Undergraduate Laboratory Internship (SULI) Program under the direction of Michael Toney and Bridget Ingham at the Stanford Synchrotron Radiation Laboratory of the Stanford Linear Accelerator Center in Palo Alto, CA.

Participant: _____

Research Advisor: _____

TABLE OF CONTENTS

Abstract	iii
Introduction	1
Materials and Methods	2
Results	3
Discussion and Conclusions	5
References	8
Figures	9

ABSTRACT

Many properties of zinc oxide, including wide bandgap semiconductivity, photoconductivity, and chemical sensing, make it a very promising material for areas such as optoelectronics and sensors. This research involves analysis of the formation, or nucleation, of zinc oxide by electrochemical deposition in order to gain a better understanding of the effect of different controlled parameters on the subsequently formed nanostructures. Electrochemical deposition involves the application of a potential to an electrolytic solution containing the species of interest, which causes the ions within to precipitate on one of the electrodes. While there are other ways of forming zinc oxide, this particular process is done at relatively low temperatures, and with the high amount of x-ray flux available at SSRL it is possible to observe such nucleation *in situ*. Additionally, several parameters can be controlled using the x-ray synchrotron; the concentration of Zn^{2+} and the potential applied were controlled during this project.

The research involved both gathering the X-ray diffraction data on SSRL beamline 11-3, and analyzing it using fit2d, Origin 6.0 and Microsoft Excel. A time series showed that both the in-plane and out-of-plane components of the ZnO nanorods grew steadily at approximately the same rate throughout deposition. Additionally, analysis of post-scans showed that as potential goes from less negative to more negative, the resulting nanostructures become more oriented.

INTRODUCTION

In recent years, zinc oxide has become a popular subject of research due to its applications in the areas of sensors [1], optoelectronic devices [2] and piezoelectric devices [3]. Wide bandgap semiconductivity, photoconductivity, and chemical sensing are just a few examples of the properties that make ZnO so useful [4]. To better understand these bulk ZnO properties, it is advantageous to create and analyze its nanostructures, which have a high surface to volume ratio and therefore enhance bulk characteristics. Several techniques have been established to form such nanostructures, including thermal evaporation of ZnO powder in the presence of a carrying gas both with a catalyst [5] and without a catalyst [6], sol-gel [7], anodic aluminum oxide templating [8], metal-organic chemical vapor deposition [9], molecular beam epitaxy [10], pulsed laser deposition [11], and electrochemical deposition [12].

Electrochemical deposition has distinct advantages for the study of nanostructures because it is more cost-effective and easier than other techniques. During the process, a potential is applied to an electrolytic solution that contains the species of interest. The ions within the solution then precipitate on the electrode. It can be done at relatively low temperatures, making deposition possible on inexpensive substrates with low melting points, such as plastics. Additionally, a vacuum system is not necessary. Electrochemical deposition allows for complete control over several parameters, including temperature, pH, presence of surfactant, concentration of Zn^{2+} and potential applied. Lastly, it can be readily scaled for industrial production.

Although electrochemical deposition provides many benefits for the study of ZnO nanostructures, there are still many aspects of the deposition that are not fully understood. While the resulting nanostructures from the deposition can easily be observed and analyzed, nothing

from the final structures tells about what exactly happened during the deposition. It is unknown precisely how the orientation of the nuclei affects the final structure. This research allows for analysis the actual deposition process, as well as the resulting nanorods to investigate why the nanorods become oriented in the way that they do and how the degree of orientation is determined.

Using x-ray diffraction techniques, an x-ray beam is aimed at the crystal lattice such that the beam is reflected onto a detector. The result is a series of peaks in intensity that are due to constructive interference of waves from different layers in the lattice. The data from the diffraction experiments give details about the preferential structure; specifically, there are different orientations and shapes that may form, such as plates and rods [13]. These different outcomes depend directly upon the different parameters that are controlled during the experiment. The effects of initial concentration of Zn^{2+} and potential applied were examined because they are most significant in determination of the final structure. Ultimately, x-ray diffraction is an ideal tool for tracking crystallite orientation and an aid in the attempt to fully understand how the orientation of the rods develops from the nuclei to the final structure.

MATERIALS AND METHODS

A homemade electrochemical cell with heating capability, as illustrated in Figure 1, was used for the diffraction process. The samples are deposited on the working electrode, which is a quartz rod with 150 nm of gold deposited on it. This rod is inserted at the base of the cell such that x-rays may be directed at grazing incidence onto the film on top of the rod, where there is a

2 mm x-ray path length through the solution. The electrochemistry is controlled while x-ray diffraction patterns are recorded by the detector

The aqueous electrolytic solution within the cell had a controlled concentration of $\text{Zn}(\text{NO}_3)_2$ (Riedel DeHaën, 98%) varying from 1-50 mM, with a supporting electrolyte of 0.1 M KCl (BDH, 99%). The temperature of the solution was held between 60-65°C during the deposition. Also used was a Pt wire counter electrode, whose potential was regulated with the use of a potentiostat and varied from -970 mV to -370 mV with respect to an Ag/AgCl/KCl (3.5 M) reference electrode (+0.205 V vs. NHE). Oxygen was bubbled through the solution at a moderate rate.

The x-ray diffraction experiments were conducted using the area detector on beam line 11-3 of the Stanford Synchrotron Radiation Laboratory at the Stanford Linear Accelerator Center, California [14]. The area detector differs from a point detector in that it gives two-dimensional, rather than one-dimensional, results. The beam size was 0.15 mm by 0.05 mm and the wavelength was 0.9736 Å.

After gathering the data, the quartz rods were taken to Imperial College London, UK to obtain microstructure images of the resulting nanostructures with the use of LEO Gemini 1525 field emission microscope (FESEM).

RESULTS

X-ray diffraction on beam line 11-3 yielded a series of radial diffraction patterns such as Figure 2. This particular scan was taken after deposition occurred and solution was removed from Sample 04 (5 mM $\text{Zn}(\text{NO}_3)_2$, -370 mV). The diffraction pattern results from the interference of waves from different layers in the lattice, as described by Bragg's Law:

$$n\lambda = 2d\sin(\theta).$$

In this equation, λ is the wavelength, d is the separation between the parallel lattice planes, 2θ is the angle between the incident beam and the scattered beam, and n corresponds to the amount of shifting between the two waves. When n is an integer, i.e. the two waves are in phase, we see a bright spot of constructive interference, or, in this case, a bright arc.

Although the pattern is in real space, as defined by the scale of pixels along the horizontal and vertical directions, we can also read it radially using Q and χ . The angle χ completes an entire circle of 360° , with 0° at the vertical, but due to experimental limitations (the x-ray beam has a limited span it can cover before the cell obstructs it) only the region from -90° to 90° is useful for analysis. The scattering vector, Q (measured in \AA^{-1}), increases radially outward. Q is related to the distance between parallel lattices (“ d ”) as follows:

$$Q = 2\pi/d.$$

We can combine it with Bragg’s Law, resulting in the following:

$$Q = (4\pi/\lambda)*\sin(\theta).$$

Each arc represents a specific orientation of either the ZnO crystals or the gold upon which it was deposited. The arcs of importance are labeled in Figure 2 as follows: ZnO (102), Au (200), Au (111), ZnO (101), and ZnO (002). By using the intensity color scale, one can see the relative intensities, measured in counts, of each orientation.

The program Fit2d was used to integrate Figure 2 in a process called caking to create the graph shown in Figure 3. This essentially changes the polar coordinates of χ and Q to Cartesian coordinates. The horizontal becomes the off-axis angle χ and the vertical is the magnitude of the scattering vector Q . Per the definition above, as Q increases on Figure 3, d decreases. Using

figure 3, one may see more easily the different diffraction peaks, which are once again labeled on the figure and are now horizontal lines.

Cuts were taken along the horizontal lines corresponding to the reflections of ZnO (102), ZnO (002), ZnO (101) and Au (111) of Figure 3 to create the four individual graphs shown in Figure 4. These graphs are now one-dimensional, with each one showing the intensity vs. χ for one specific orientation. They are offset for clarity.

The peaks in Figure 4 can be fitted with Gaussian curves to obtain the area, which corresponds to the degree of crystallinity along the different directions, the center, and FWHM (Full Width at Half Maximum), which tell us about the strength of the scattering and the variation in texture (preferential orientation).

DISCUSSION AND CONCLUSIONS

The different orientations that could be analyzed using the x-ray diffraction pattern of Figure 2 are ZnO (002), ZnO (102), ZnO (101), Au (111) and Au (200), which are all labeled in Figures 2 and 3. These orientations correspond to Miller Indices; each represents a combination of either in-plane or out-of-plane components. As shown in Figure 5, Au (111) is directed normal to the gold substrate, while ZnO (002) component of the hexagonal ZnO nanorod that is also perpendicular to the substrate. ZnO (100) gives a component entirely in the plane of the substrate. Lastly, ZnO (102) and ZnO (101) are combinations of the in-plane and out-of-plane components.

1. End-Scan Crystallinity

The first goal achieved during analysis was to look for correspondence between the potential applied and the degree of orientation of the full-grown nanostructures using the FWHM

of the end-scans for samples formed with $\text{Zn}(\text{NO}_3)_2$ concentration of 1 mM at potentials of -970 mV, -770 mV and -370 mV. The FWHM from the Gaussian fits for the ZnO (102) intensity peaks were used for this part of the analysis. Each FWHM corresponds with the amount of variation in crystallite (grain) direction about the midpoint. A greater width is the result of a larger distribution of grain orientation, i.e. less orientation of the grains. On the other hand, a very small width is caused by a highly oriented material. Figure 6 is a graph of the width of the ZnO (102) intensity peak (measured in degrees χ) vs. potential applied in mV for the three samples described above. When moving from less negative potential (-370 mV) to more negative potential (-970 mV), the width decreases, meaning the grains are more structurally ordered. These results are very encouraging in their strong suggestion that the degree of crystallinity of ZnO nanostructures can be controlled by the potential applied during electrochemical deposition. Further studies similar to this—possibly ones that include more than four applied potentials—would be useful in providing more support for this conclusion.

2. Time-Series Analysis

A second aspect analyzed during this research project is a time series for one of the samples. For this analysis Gaussian fits were used for all 26 scans that took place during the deposition of the ZnO in a sample formed using 1 mM $\text{Zn}(\text{NO}_3)_2$ at -370 mV. The time scans allow one to look at each step of the growth process.

The ZnO (002) and the ZnO (101) peaks were used during this analysis. The areas of the peaks allowed comparison of the growth of the nanostructures normal to the substrate with the growth in the plane of the substrate. Figures 7 and 8 show the area ratio (the areas were scaled down for clarity) of the ZnO (002) and ZnO (101) peaks, respectively. A linear fit on each graph shows that they both are linearly increasing with time. In other words, Figures 7 and 8 show that

the nanostructures are growing steadily as time increases during deposition. Note that potential was applied starting at scan 5. Accordingly, the plots show no amount of substance until scan 6 (for ZnO (002)). Interpolation from the linear fit shows that the first point at which substance was detected is about halfway through scan 5. Each scan was about one minute long; therefore, nucleation time is approximately 30 seconds.

Note that there are a few small jumps in the data, specifically in the ZnO (101). These jumps are actually apparent in both orientations but more prominently so in the ZnO (101), which is likely to be due to the poor signal-to-noise ratio. The jumps may be caused by sudden increases in oxygen near the electrode. Further analysis of these jumps will be beneficial in the future.

Figure 9 combines Figures 7 and 8 to show that the rate of growth is nearly identical in both directions. The graphs correspond quite well with previous data collected during XANES analysis at Brookhaven National Laboratory [15, 16]. During deposition of ZnO using identical conditions, the XANES time series for the less negative potentials resulted in a nearly linear volume increase.

Future analysis will include doing time series for more of the samples from this experiment and comparing the results. It is expected that the time series of scans at more negative potentials will show more rapid growth than this one. Furthermore, it is predicted that at more negative potentials there will ultimately be more growth in the (002) orientation than the (101) orientation [15, 16]. Future research also includes obtaining the FESEM images from Imperial College London, UK, to use as a supplement to the above results and conclusions.

ACKNOWLEDGMENTS

There are several people who have helped me immensely during this project. I am most especially thankful for the intelligence, guidance and support provided by my mentors, Michael Toney and Bridget Ingham. Additional thanks to our collaborators Benoit Illy and Mary Ryan. I would also like to thank Apurva Mehta, for going out of his way to help out all of the SSRL interns. Lastly, I would like to thank the Office of Science, Department of Energy for funding the SULI program and all of the SULI coordinators at SLAC for making this experience possible.

REFERENCES

- [1] Q. Wan, Q.H. Li, Y.J. Chen, T.H. Wang, X.L. He, J.P. Li and C.L. Lin, *Appl. Phys. Lett.* 84 (2004) 3654.
- [2] M. Law, L.E. Greene, J.C. Johnson, R. Saykally and P.D. Yang, *Nat. Mater.* 4 (2005) 455.
- [3] M. Kadota, T. Miura, *Jpn. J. Appl. Phys.* 41 (2002) 3281.
- [4] B. Illy, B. A. Shollock, J.L. MacManus-Driscoll, M.P. Ryan, *Nanotechnology* 16 (2005) 320.
- [5] X.Y. Kong, Y. Ding, R. Yang and Z.L. Wang, *Science* 303 (2004) 1348.
- [6] Z.W. Pan, Z.R. Dai, and Z.L. Wang, *Science* 291 (2001) 1947.
- [7] B.B. Lakshmi, P.K. Dorhout and C.R. Martin, *Chem. Mater.* 9 (1997) 857.
- [8] Y. Li, G.W. Meng, L.D. Zhang and F. Philip, *Appl. Phys. Lett.* 76 (2000) 2011.
- [9] J.Y. Park, D.J. Lee, Y.S. Yun, J.H. Moon, B.T. Lee and S.S. Kim, *J. Cryst. Growth* 276 (2005) 158.
- [10] H. Kato, M. Sano, K. Miyamoto and T. Yao, *J. Cryst. Growth* 237-239 (2002) 538.
- [11] T. Okada, B.H. Agung and Y. Nakata, *Appl. Phys. A* 79 (2004) 1417.
- [12] M.H. Wong, A. Berenov, X. Qi, M.J. Kappers, Z.H. Barber, B. Illy, Z. Lockman, M.P. Ryan, J.L. MacManus-Driscoll, *Nanotechnology* 14 (2003) 968.
- [13] Z. R. Tian, J.A. Voigt, J. Liu, B. Mckenzie, M.J. Mcdermott, M. A. Rodriguez, H. Konishi, H. Xu, *Nat. Mater.* 2 (2003) 821.
- [14] RCSB Protein Data Bank, Structural Biology Synchrotron Users Organization, 2006, <http://biosync.rcsb.org/ssrl/BL11-3.html>
- [15] B. Ingham, B. N. Illy, J. R. Mackay, S. P. White, S. C. Hendy, M. P. Ryan, *Mat. Res. Soc. Symp. Proc.* 1017 (2007) DD12.16
- [16] B. Ingham, B. N. Illy and M. P. Ryan, *J. Phys. Chem. C* (submitted)

FIGURES

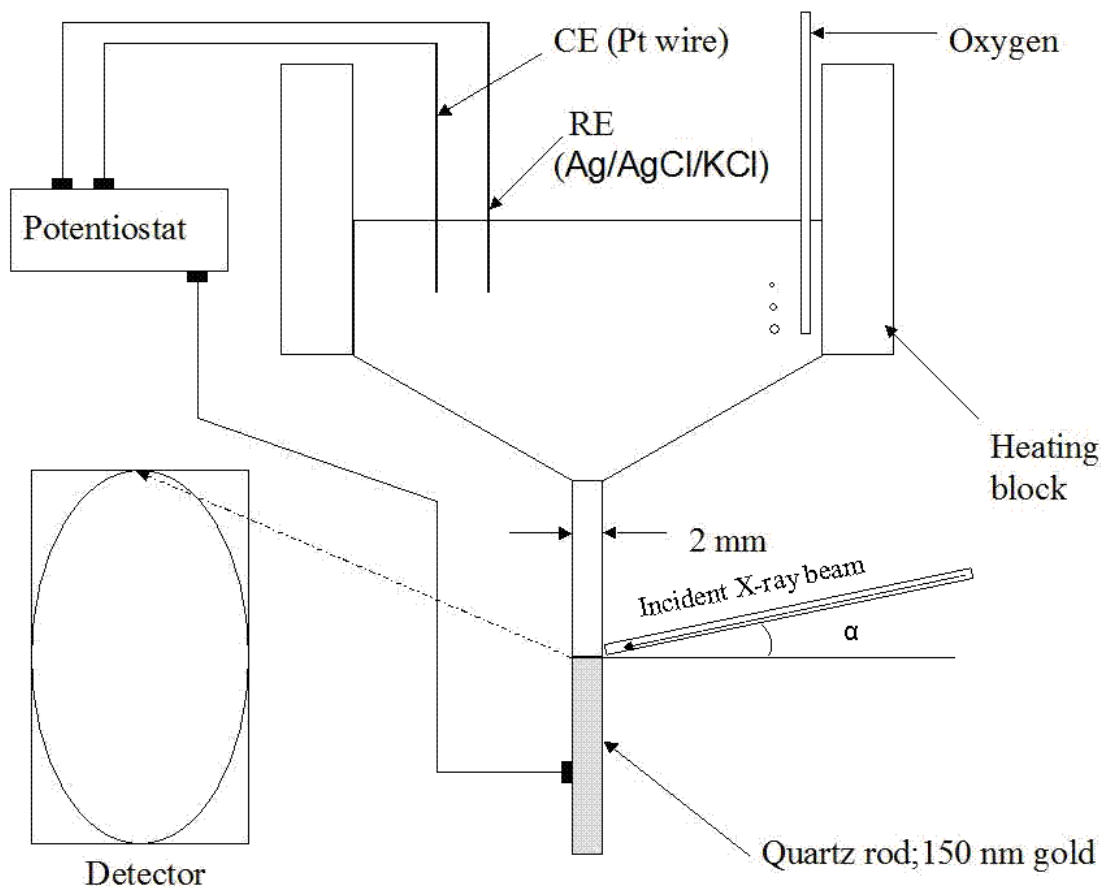


Figure 1: Schematic diagram of experimental setup. CE is counter electrode; RE is reference electrode. The electrochemistry is controlled as the x-ray beam reflects off the top of the quartz rod (working electrode) and onto the detector. The beam is directed at grazing incidence, meaning that the angle α is very small ($\sim 0.1^\circ$).

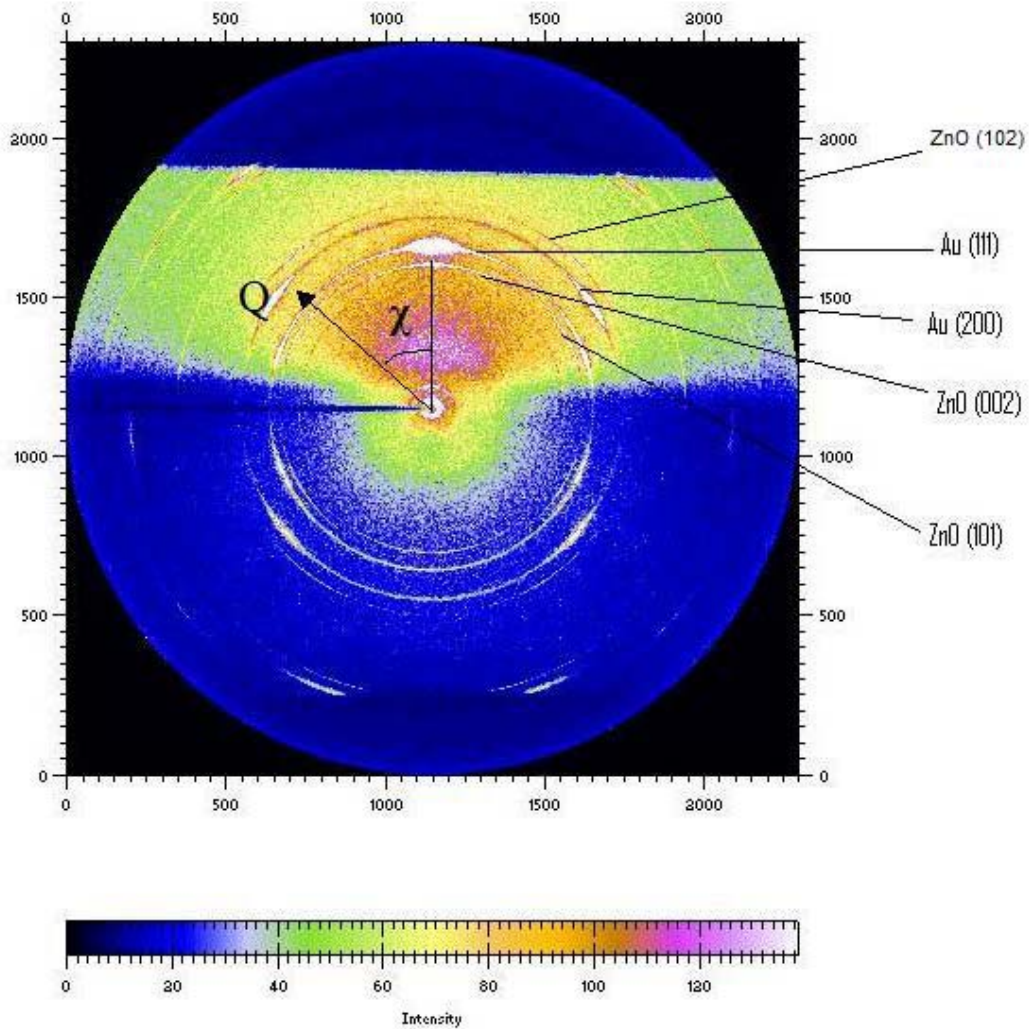


Figure 2: This is the diffraction pattern from an end scan (solution has been removed). Each intensity peak corresponds with a specific orientation of either ZnO or Au, as labeled. Areas colored blue were not used for analysis because the cell was in the way of the x-ray beam. The data can be read in polar coordinates by using the angle χ from the vertical and the scattering vector Q .

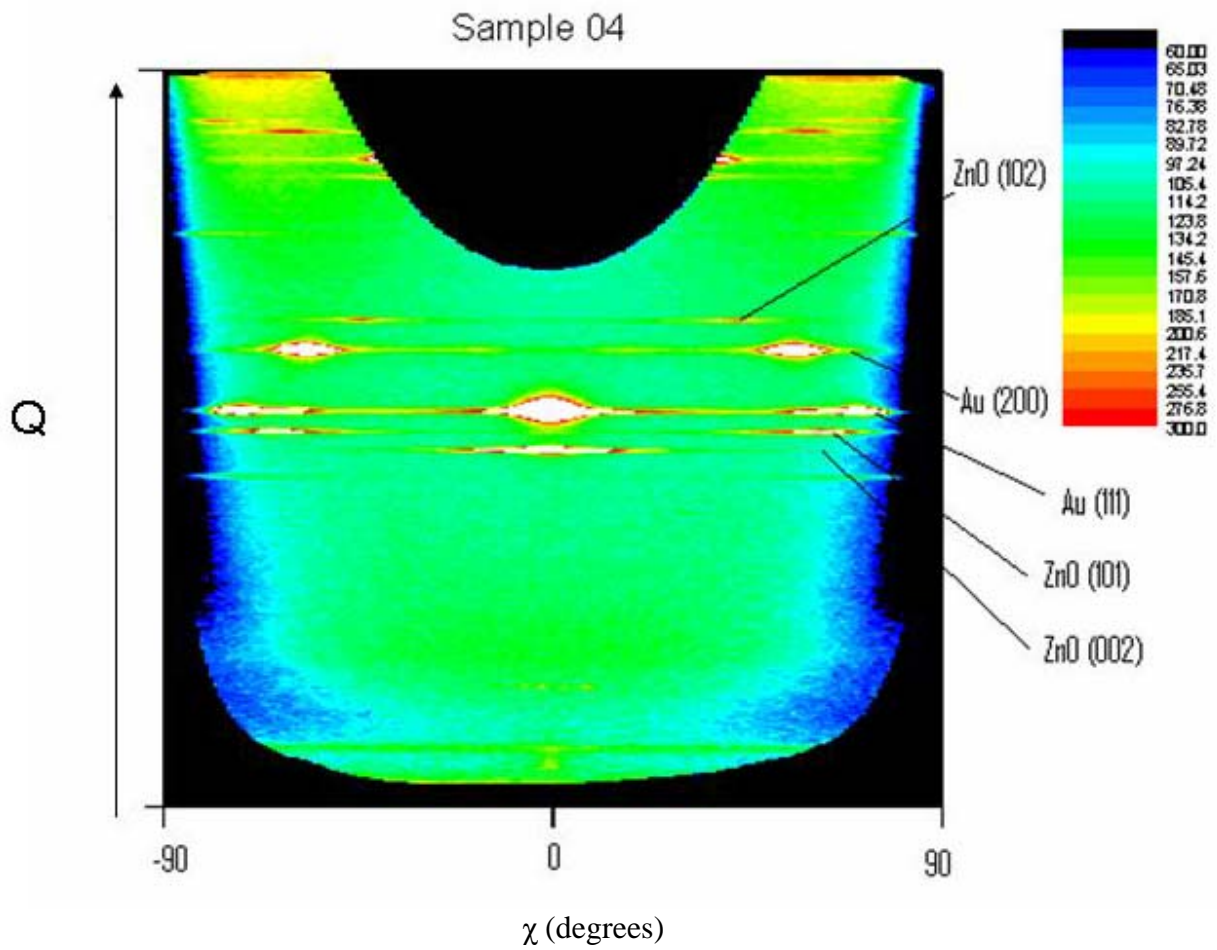


Figure 3: The raw data from Figure 2 has been caked in Fit2d to create this graph, in which χ is now the horizontal axis and Q is the vertical axis. The result is that the arcs containing the intensity peaks for the different orientations are now horizontal lines.

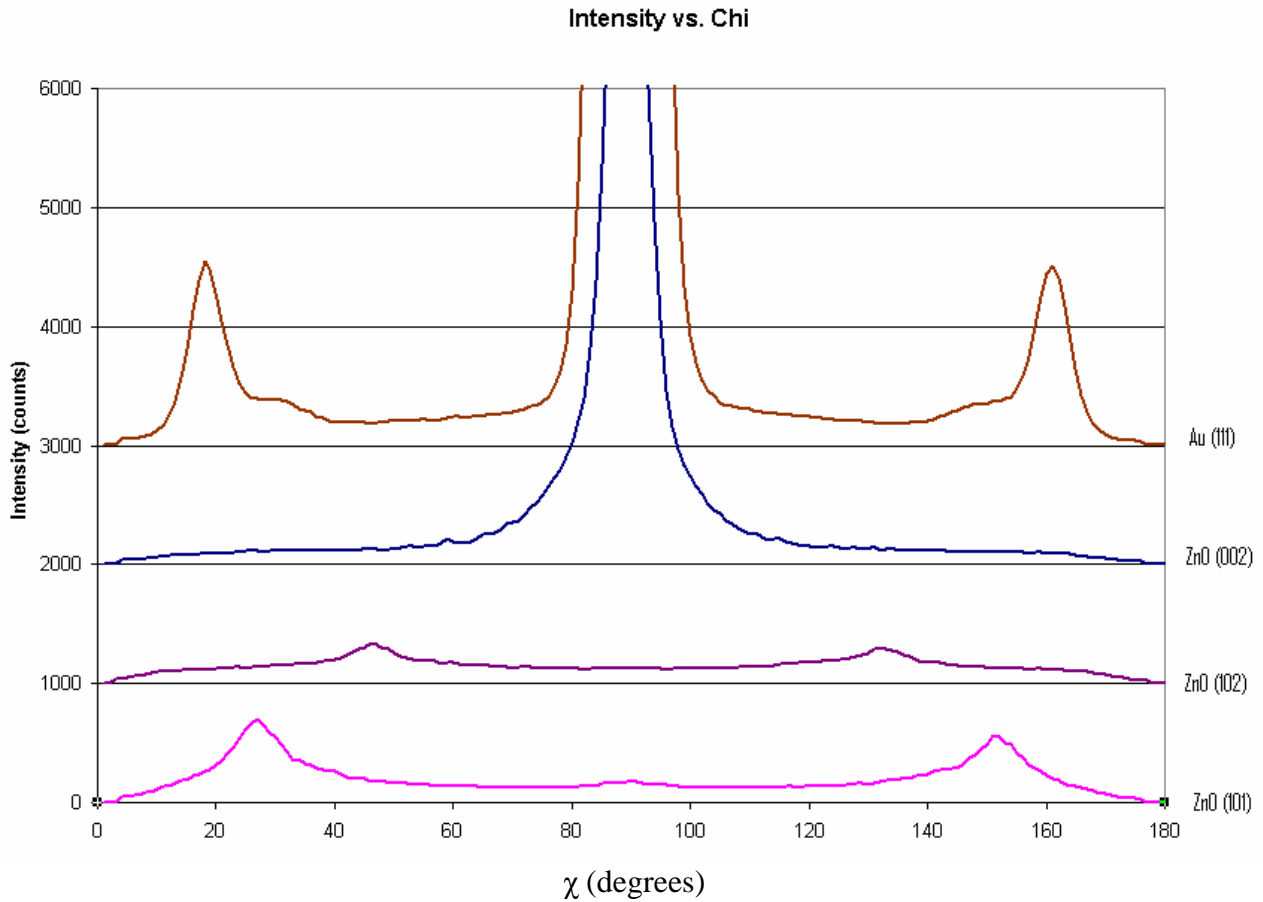


Figure 4: A cut was taken along the horizontal row of maximum intensity for each orientation of interest in the caked image of Figure 3. These cuts were used to create this graph of intensity vs. χ , which shows the individual intensity peaks for each orientation. The graph is offset for clarity.

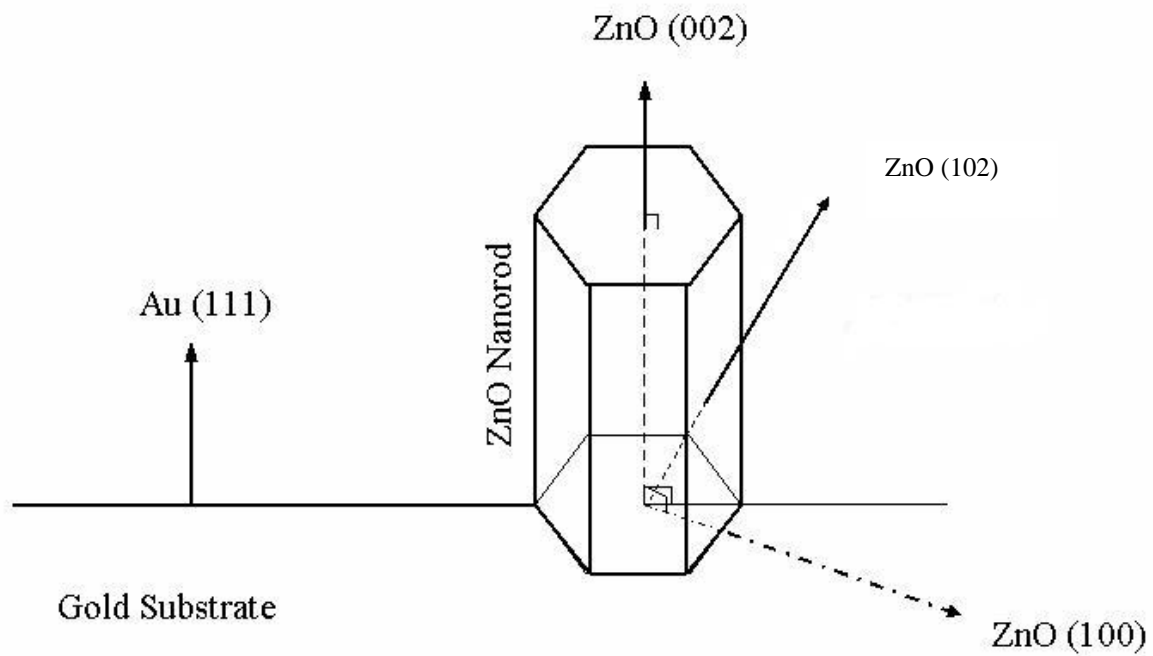


Figure 5: Several orientations are labeled in this diagram. The Au (111) orientation is straight off the substrate, while the different ZnO orientations correspond with in-plane and out-of-plane components of the hexagonal zinc oxide nanorods.

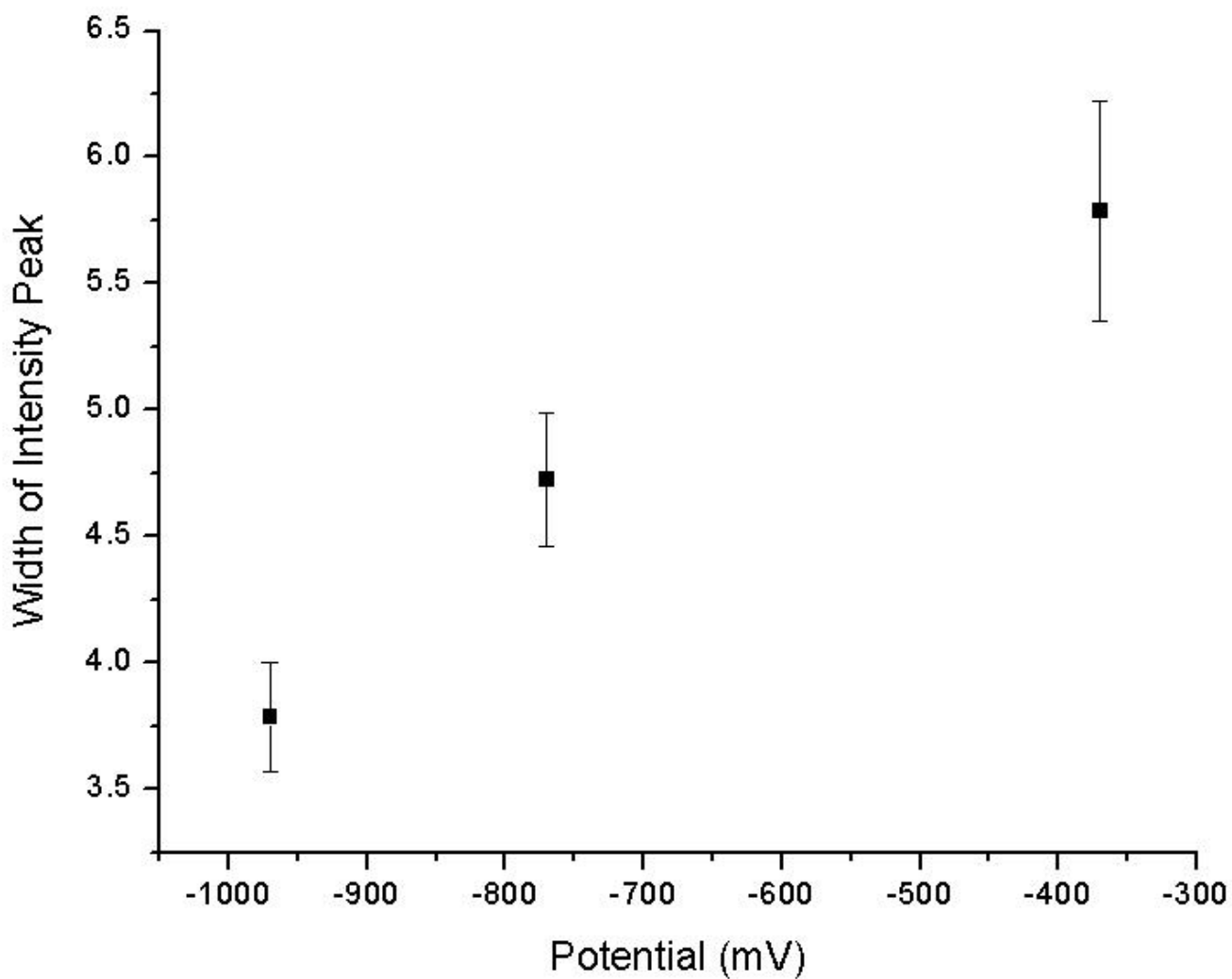


Figure 6: This is a plot of the width of the ZnO (102) intensity peak vs. the potential applied to the electrochemical solution. The width of the intensity peak (see Figure 4 for intensity peaks) is measured in degrees of χ .

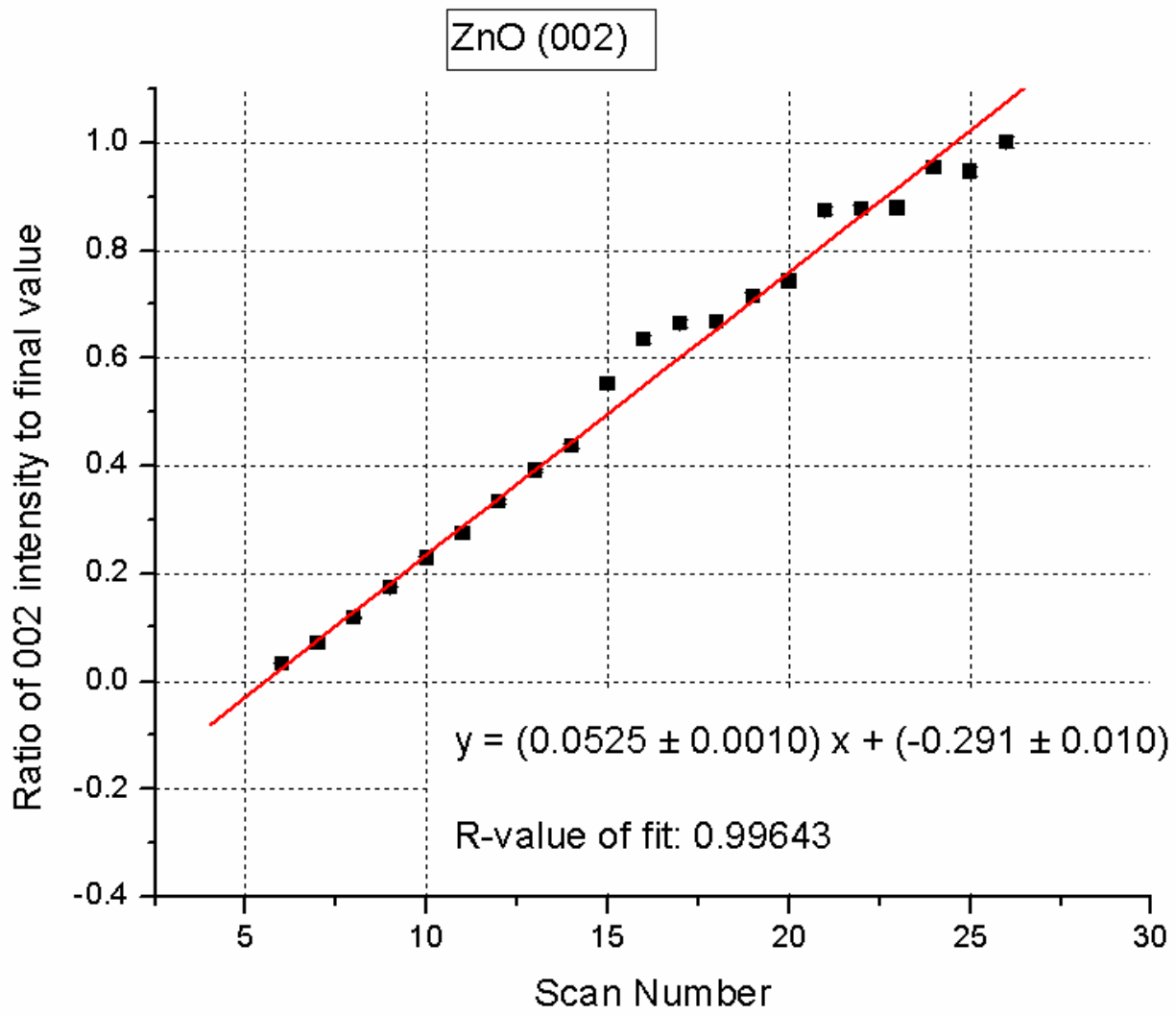


Figure 7: The area of the ZnO (002) intensity peak was divided by 48,789. The linear fit of the plot indicates steady growth over time.

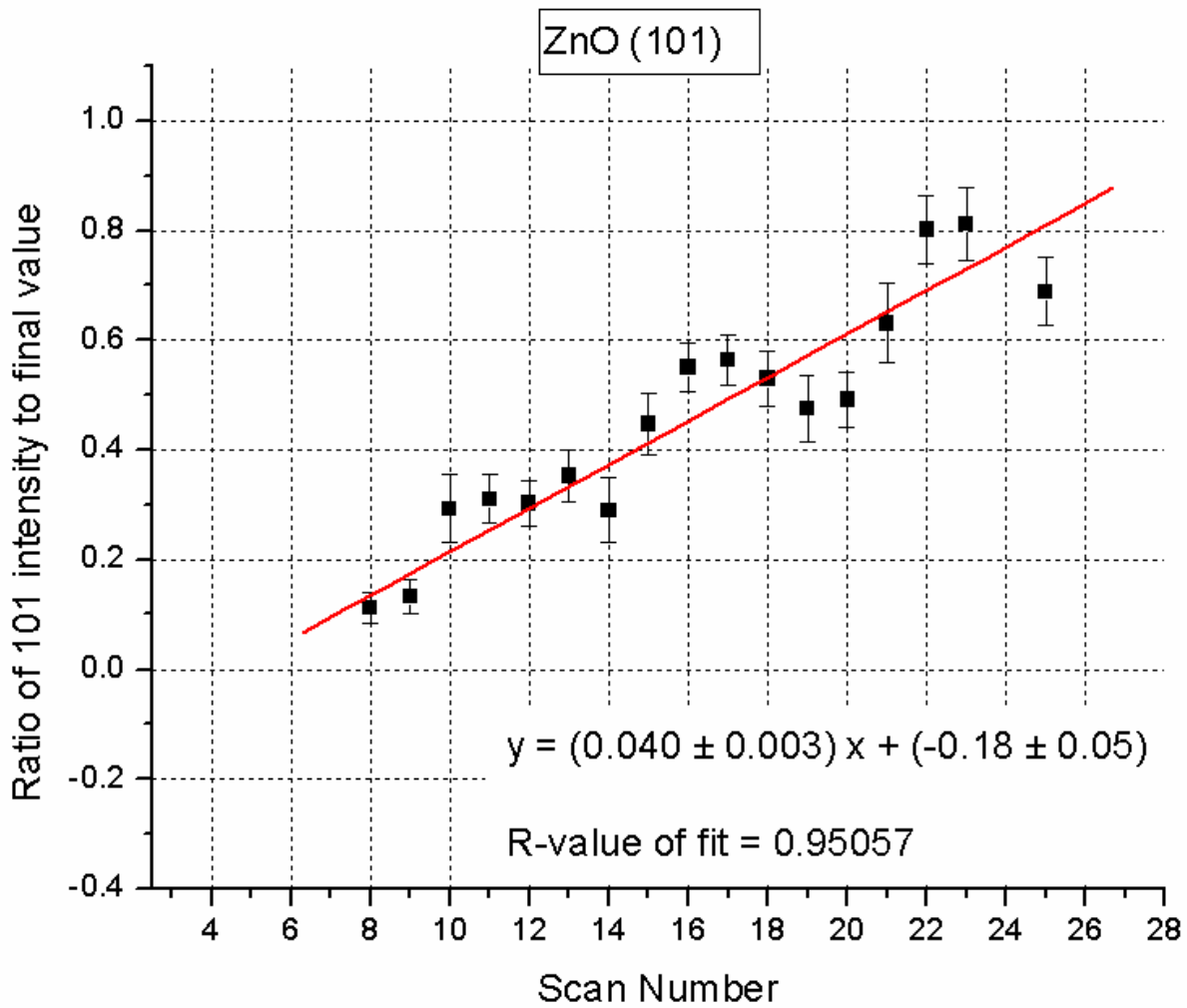


Figure 8: The area of the ZnO (101) intensity peak was divided by 1,600. The linear fit of the plot indicates steady growth over time.

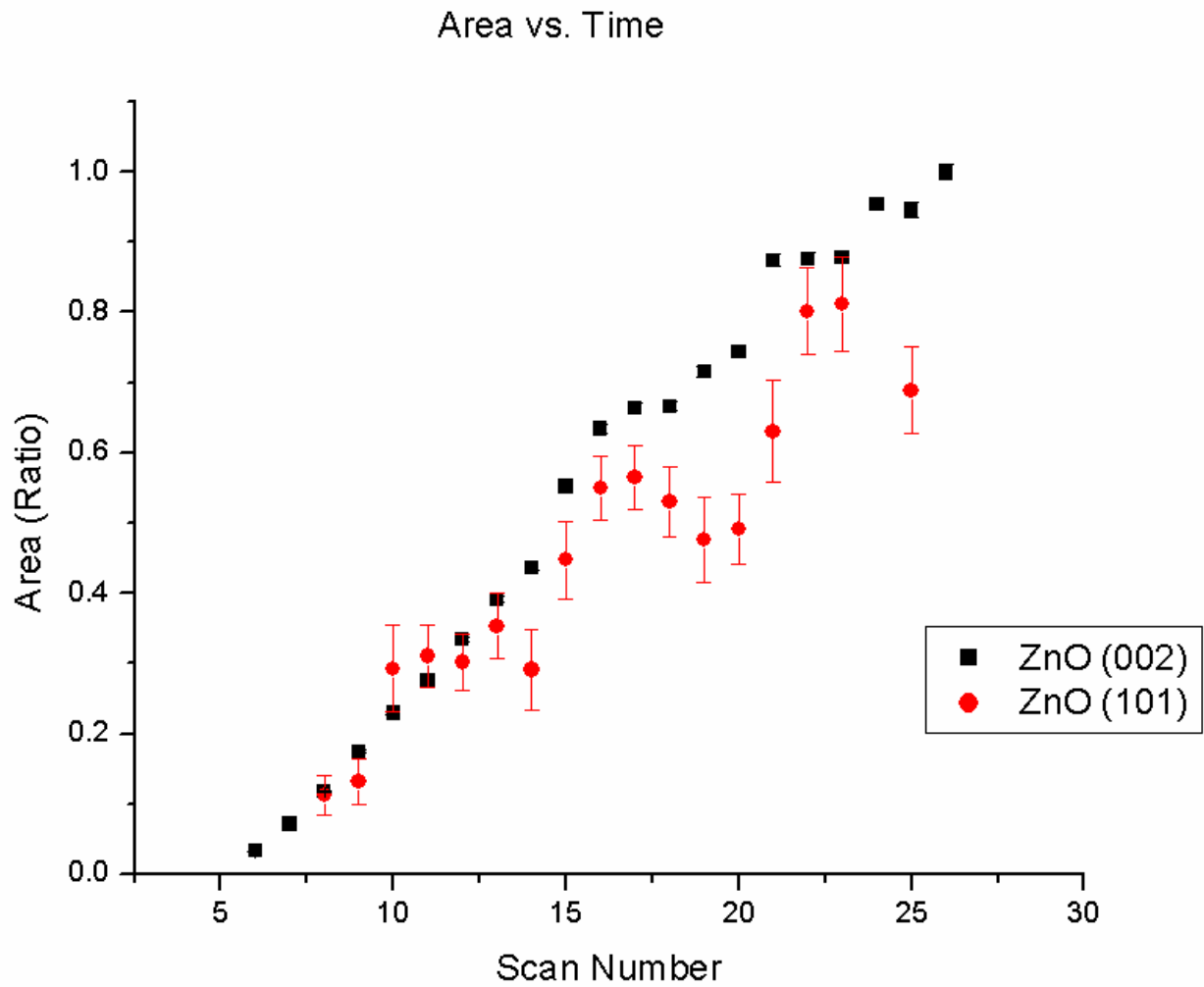


Figure 9: This area vs. scan number plot is merely a combination of Figures 7 and 8. It shows how the areas of both the ZnO (002) and the ZnO (101) change over time. Both orientations are scaled for clarity: ZnO (002) is scaled by a factor of 48,789 while ZnO (101) is scaled by a factor 1600.